[11] W. Fu and E. L. Tan, "A parameter optimized ADI-FDTD method based on the (2, 4) stencil," *IEEE Trans. Antennas Propag.*, vol. 54, no. 6, pp. 1836–1842, Jun. 2006.

[12] T. Hirono, W. W. Lui, and K. Yokoyama, "Time-domain simulation of electromagnetic field using a symplectic integrator," *IEEE Microw. Guided Wave Lett.*, vol. 7, no. 9, pp. 279–281, Sep. 1997.

[13] I. Saitoh, Y. Suzuki, and N. Takahashi, "The symplectic finite difference time domain method," *IEEE Trans. Magn.*, vol. 37, no. 5, pp. 3251–3254, Sep. 2001.

[14] S.-Y. Zhong, X. Wu, S.-Q. Liu, and X.-F. Deng, "Global symplectic structure-preserving integrators for spinning compact binaries," *Phys. Rev. D*, vol. 82, no. 12, p. 124040, Dec. 2010.

[15] W. Sha, Z. Hang, M. S. Chen, and X. L. Wu, "Survey on symplectic finite-difference time-domain schemes for Maxwell's equations," *IEEE Trans. Antennas Propag.*, vol. 56, no. 2, pp. 493–500, Feb. 2008.

[16] S. Liu, Z. He, S. Cheng, and S.-Y. Zhong, "Symplectic finite-difference time-domain scheme based on decomposition technique of the exponential operator for plasma media," *IET Microw., Antennas, Propag.*, vol. 10, no. 2, pp. 129–133, Jan. 2016.

[17] Z. Su, Y. Yang, J. Tan, and Y. Long, "A parameter-optimized symplectic FDTD method based on the (4, 4) stencil," *IEEE Antennas Wireless Propag. Lett.*, vol. 12, no. 7, pp. 894–897, Jul. 2013.

[18] S. Y. Zhong and S. Liu, "The force-gradient symplectic finite-difference time-domain scheme for Maxwell's equations," *IEEE Trans. Antennas Propag.*, vol. 63, no. 2, pp. 834–838, Feb. 2015.

[19] L. I. Schiff, *Quantum Mechanics*. London, U.K.: McGraw-Hill, ch.14, 1968.

[20] J. Xu and X. Wu, "Several fourth-order force gradient symplectic algorithms," *Res. Astron. Astrophys.*, vol. 10, no. 2, pp. 173–188, Feb. 2010.

[21] F. Casas and A. Murua, "An efficient algorithm for computing the Baker–Campbell–Hausdorff series and some of its applications," *J. Math. Phys.*, vol. 50, no. 3, p. 033513, Mar. 2009.

[22] R. D. Ruth, "A canonical integration technique," *IEEE Trans. Nucl. Sci.*, vol. 30, no. 4, pp. 2669–2671, Aug. 1983.

[23] R. I. McLachlan and P. Atela, "The accuracy of symplectic integrators," *Nonlinearity*, vol. 5, no. 2, pp. 541–562, 1992.

[24] A. Taflove, *Computational Electrodynamics: The Finite-Difference Time-Domain Method*. Norwood, MA, USA: Artech House, 1995.

[25] D. M. Sheen, S. M. Ali, M. D. Abouzahra, and J. A. Kong, "Application of the three-dimensional finite-difference time-domain method to the analysis of planar microstrip circuits," *IEEE Trans. Microw. Theory Techn.*, vol. 38, no. 7, pp. 849–857, Jul. 1990.

[26] J.-P. Berenger, "Three-dimensional perfectly matched layer for the absorption of electromagnetic waves," *J. Comput. Phys.*, vol. 127, no. 2, pp. 363–379, Sep. 1996.

Horizontally Polarized Omnidirectional Antenna Array Using Cascaded Cavities

Le Chang, Yue Li, Zhijun Zhang, and Zhenghe Feng

Abstract—A new structure of horizontally polarized (HP) antenna array is presented for azimuthal omnidirectional coverage. The proposed antenna array is engineered by breaking the fringing field symmetry along the typical parallel strip-lines, which is implemented by loading field-block structures alternatively and periodically. In physics, the blocking structures constrain the fringing fields inside, producing a series of rectangular open cavities operating at the TM_{1n0} ($n = 0.5$) mode. Counterintuitively, these asymmetric open cavities are able to generate an omnidirectional radiation pattern in the E plane with horizontal polarization, similar to the linear magnetic current array. In order to verify the design strategy, a five-unit center-fed cascaded cavity array is fabricated and tested. The measured bandwidth is 120 MHz (5.83–5.95 GHz) with reflection coefficient lower than -10 dB. The HP omnidirectional pattern at 5.9 GHz provides a gain variation of 1.94 dB ranging from 6.7–8.64 dBi.

Index Terms—Antenna arrays, antenna radiation patterns, azimuthal omnidirectional pattern, cascaded cavities, horizontal polarization.

I. INTRODUCTION

Omnidirectional antennas are needful for Wireless Local Area Network (WLAN) access point and portable devices in order to acquire a large service area. A large amount of omnidirectional antennas have been studied. Vertically polarized omnidirectional antennas, such as the traditional dipole, dipole array [1], dual-band dipole [2] and its array [3], coaxial collinear antenna [4], and wideband segmented dipole [5], have been studied for many years. However, in the urban or indoor wireless environment, the vertical polarization may change significantly after multiple diffraction, and Soras *et al.* [6] and Chizhik *et al.* [7] have reported that using horizontally polarized (HP) antennas results in 10-dB more power compared to the case where vertically polarized antennas are used. Therefore, HP omnidirectional (HPO) antennas are preferable for WLAN applications.

The wire-type Alford loop antenna was the first kind of HPO antenna [8]. Several planar Z-shaped or circular ring antennas have been reported to produce uniform currents along the loops based on the Alford loop [9]–[13]. A zeroth-order HP loop antenna with a perimeter of one wavelength achieves uniform current and good impedance matching by loading left-handed components [14]. The current along the loop with a perimeter of several fold wavelengths may flow in the same direction and remain in phase if the loop consists of a number of segmented smaller loops [15]. Based on this principle, three electrically large loop antennas with HPO patterns have been introduced [15]–[18]. Other than various loop antennas, wideband HPO patterns were achieved by arranging four HP folded
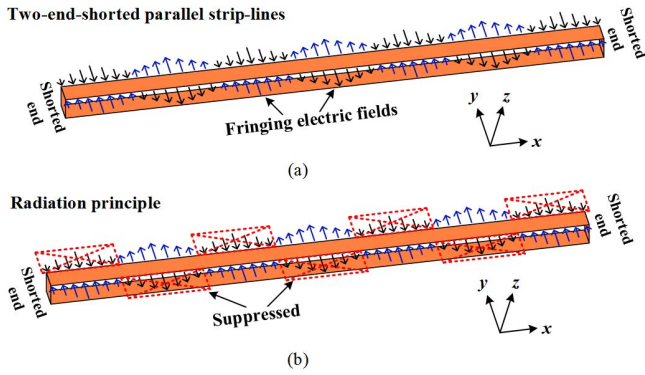
Fig. 1. (a) Fringing electric fields of the two-end-shorted parallel strip-lines. (b) Schematic diagram of the radiation principle. Red dotted cross-lines in parallelograms: suppression of the "dark fields."

dipoles around a square box [19]. However, the 3-D structure is bulky. Moreover, a rectangular open cavity antenna excited by two slots on its sidewall [20] and a circular array consisting of eight tapered slots [21] can produce HPO patterns. However, it is difficult to form linear arrays using the abovementioned HPO antennas. The substrate integrated waveguide (SIW) double-sided slot array is another approach to achieve HPO pattern, and this kind of antenna effectively overcomes this problem [22], [23].

In this communication, a new structure of the rectangular open cavity cascaded antenna based on the parallel strip-lines (PSL) is proposed to produce the HPO pattern. Here, by loading field-block structures to the two-end-shorted PSL alternatively and periodically, the fields along one direction are suppressed while along the other direction they are left with an identical phase, forming a linear magnetic current array, and consequently, generating omnidirectional pattern in the E plane. From the field standpoint, the TM_{1n0} ($n = 0.5$) mode standing wave is resonant within each open cavity, resulting in a novel cavity cascaded antenna. Thus, a center-fed five-unit cavity cascaded HPO antenna is designed and fabricated. It provides a bandwidth of 120 MHz and an HPO pattern with a maximum gain of 8.67 dBi and gain variation of less than 2.04 dB in the passband.

II. RADIATION AND OMNIDIRECTION PRINCIPLES

A. Starting Point: Two-End-Shorted Parallel Strip-Lines

The schematic diagram of the radiation principle of the two-end-shorted PSL is illustrated in Fig. 1. The fringing electric fields of the two-end-shorted PSL are given in Fig. 1(a): standing-wave-type fields are distributed along the line, and the fields on one side are out of phase with their counterparts on the other side, as depicted in Fig. 1 (blue and dark arrow lines) (named the "dark/blue fields"). So the wave is confined and resonant between the lines. However, as shown in Fig. 1(b), if the fields along one direction, such as the dark fields, are suppressed using some approach, then the blue fields are left, leading to effective radiation. According to the "LOVE equivalent theorem," the radiation is equivalent to a series of the magnetic currents, which are almost in-line. In addition, the linear magnetic current array is able to expand to achieve more gains.

B. Realization and Field Distributions

Fig. 2(a) shows the exploded view of the realization of the magnetic current array. The two-end-shorted PSL is printed in a single F4B substrate board whose permittivity is 2.55 and whose loss tangent is less than 0.001. A series of blocking structures, which are used to suppress the "dark fields," are loaded to the PSL alternatively.
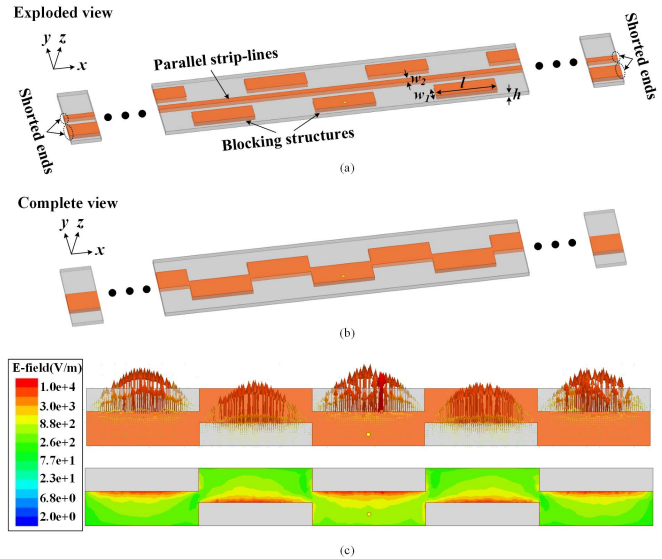

Fig. 2. (a) Exploded view and (b) complete view of the realization of the magnetic current array. (c) Complex and vector field distributions at 5.8 GHz (the antenna dimensions are $l = 29.6$ mm, $w_1 = 6$ mm, $w_2 = 3$ mm, and $h = 2$ mm).

TABLE I
GAIN VARIATION OF DIFFERENT ANTENNA SHAPE

w/mm	l/mm	d/mm	$|S_{11}|$/dB	Gain variation/dBi
9	29.6	4.5	-22.9	7.21-7.85(0.64)
11	22.1	6.0	-27.8	6.42-6.87(0.45)
13	18.7	8.0	-21.2	5.79-6.28(0.49)
15	16.1	10.8	-26.2	5.08-5.70(0.62)

*Numbers in the brackets indicate the out-of-roundness values.

The blocking structure is a cuboid with its three sidewalls removed except for the two fringe blocking structures, and the opening facing the shorted sidewall is connected to the PSL. The two fringe blocking structures' endmost sidewalls are not removed, aiming to form the pure field modes required for effective radiation. The complete view of the antenna is shown in Fig. 2(b): these cuboid blocking structures are connected to the central strips, integrating into a whole.

An example of a five-unit magnetic current array antenna is shown in Fig. 2(c), and the simulated complex and vector electric field distributions are given. The antenna dimensions are given in the annotation, and the center frequency is 5.8 GHz. As seen from the vector fields, the fringing fields of each unit flow in the same direction and has identical phase, just as what Fig. 1(b) shows. As seen from the complex fields, the field mode of each unit is the same: there exists a half-period wave along the x-direction and a quarter-period wave along the y-direction. This means that each unit is a rectangular open cavity operating at the TM_{1n0} ($n = 0.5$) mode.

It is worth mentioning that the cavity unit width is the sum of the widths of the blocking structure and PSL, and the width of the PSL is in fact the connection overlapped width of the neighboring cavities. The PSL width hardly affects the antenna performance when it is far smaller compared to the cavity width. The result is omitted here for brevity.

C. Physical Mechanism of the HPO Pattern

The schematic radiation mechanisms of the rectangular open cavity compared with the slot antenna in a finite ground are presented
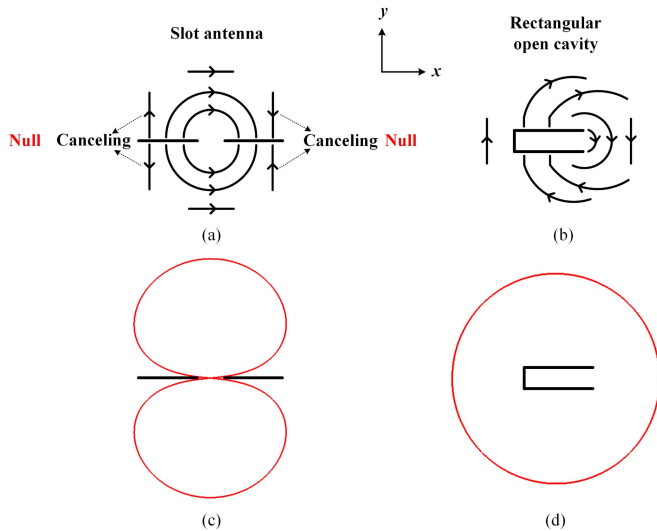
Fig. 3.   Schematic radiation mechanisms of (a) slot antenna in a finite ground and (b) rectangular open cavity. Dark arrow lines: electric fields. Radiation patterns in the E plane of the (c) slot antenna and (d) rectangular open cavity.
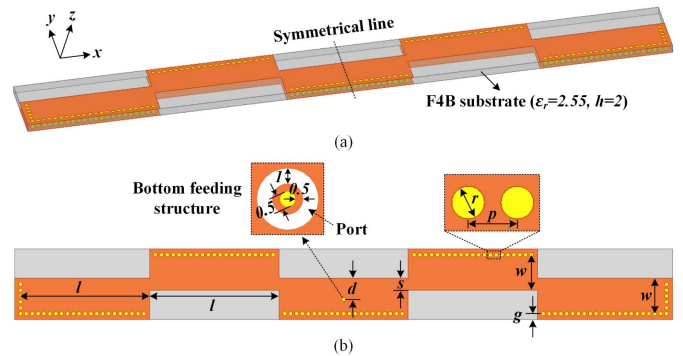

Fig. 4.   Geometry of the proposed five-unit HPO cavity cascaded antenna array. (a) Perspective view. (b) Top view. Unit all in millimeter.

TABLE II

GAIN VARIATION WITH DIFFERENT UNIT NUMBERS UNDER THREE DIFFERENT ANTENNA HEIGHTS (UNIT: dBi)

h/mm N	1	2	3
5	7.55-8.11(0.56)	7.15-7.79(0.64)	6.87-7.67(0.8)
9	9.85-10.47(0.62)	8.90-9.99(1.09)	8.64-9.44(0.8)
13	11.06-11.69(0.63)	10.09-10.68(0.59)	8.88-9.95(1.07)
17	11.50-12.10(0.6)	10.19-10.76(0.57)	9.04-9.98(0.94)
21	11.64-12.28(0.64)	10.28-10.90(0.62)	9.22-10.01(0.79)

*Numbers in the brackets indicate the out-of-roundness values.

in Fig. 3. The dark arrow lines denote the electric fields. As shown in Fig. 3(a), the electric fields emitting from the slot propagate along the ground, and the fields above and below the ground flow along opposite directions. When the fields arrive at the ground edge, they cancel each other out, leading to two nulls in radiation pattern along the $\pm x$-directions. Thus, the resultant E plane pattern has a figure-8 shape, as shown in Fig. 3(c). However, the case of the rectangular open cavity is different. As depicted in Fig. 3(b), along the $+x$-direction, the opening radiates out directly, and along the $-x$-direction, the fields above and below the cavity achieve constructive interference. As a result, an omnidirectional pattern in the E plane is obtained as shown in Fig. 3(d).

Therefore, by cascading a series of TM$_{1n0}$ ($n = 0.5$) mode rectangular open cavities alternatively, the HPO antenna array is obtained. Detailed mode analysis has been explained in [24]: the N-order mode of the N-unit antenna array is the operation mode required. The antenna in [24] was based on the microstrip line structure, with the aim of obtaining a broadside beam. Here, the proposed structure is on the basis of the PSL, as the aim is to acquire an omnidirectional beam.

III. ANTENNA DISCUSSION

In this section, the antenna performances of different antenna shapes, and the array scalability are studied. Then the design guideline is given. The antenna is designed using the software high frequency structure simulator (HFSS) version 14.

A. Relation Between Antenna Shape and Gain Variation

The gain variation of the five-unit HPO cavity cascaded antenna array at 5.8 GHz of different antenna shapes is studied, and the result is presented in Table I. Dimension illustration is depicted in Fig. 4(b). When the cavity unit width varies from 9 to 15 mm, the cavity unit length and feeding location are adjusted to acquire the impedance matching better than −20 dB at 5.8 GHz, which is shown in Table I together with the feeding locations. When the unit width decreases from 15 to 9 mm, the whole antenna shape becomes increasingly longer and narrower, the out-of-roundness are all less than 0.7 dB,

but the gain increases by more than 2 dB. Note that the out-of-roundness is calculated using the maximum and minimum gains of the E plane (yz plane). The gain increase is caused by the fact that with the decrease of the unit width, the cavity length increases, so the array factor grows while the element factor is almost identical. However, further decreasing the cavity width will make it difficult to excite the antenna array. Therefore, the cavity unit width of 9 mm is selected considering the gain as the priority.

B. Scalability

The directivity variation of the HPO cavity cascaded antenna array with different unit numbers under three different heights is investigated, and the results are shown in Table II. It is worth to mention that under each height case, the dimension of the cavity unit is adjusted separately to achieve good matching condition at 5.8 GHz. When simulating the directivity, the feeding probes all locate at the edge, that is, the maximum electric field positions, of their respective center cavity. As shown, the out-of-roundness of all cases is within 1.1 dB. The directivity increases with the increase in cavity number, and the increase rate becomes progressively slower. When the cavity number is 21, the maximum directivities approach 10–12 dBi when the heights are 3, 2, and 1 mm, respectively. This is caused by the fact that the radiation ability of the radiating cavity unit gets stronger with the increase in height. As listed in Table II, when the height of the antenna is 3 mm, the gain is without obvious increment after the cavity unit number exceeds 13. For the antenna with a larger number of unit, the energy is almost radiated without feeding into far away units. Therefore, the units at the two ends have little contribution to the antenna directivity. With the height decreases, the radiation ability of each radiating unit becomes weak, so more energy will spread to both sides, resulting in a much more uniform aperture, consequently, a higher directivity is obtained. On the other hand, the bandwidth decreases with the decrease in height. A compromised height of 2 mm is selected.
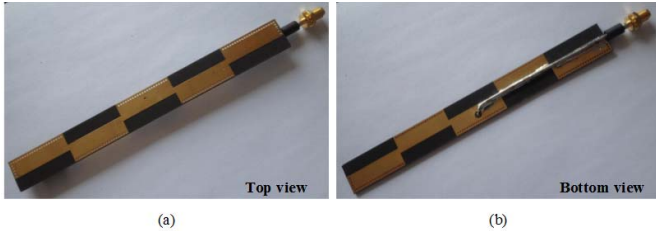
Fig. 5. Fabricated prototype. (a) Top view. (b) Bottom view.

C. Design Guideline

The guideline of designing a single-fed HPO cavity cascaded antenna array whose peak gain is less than 12 dBi is summarized as follows. If higher gain is desired, a larger antenna array excited using multiple feeds may be satisfied, and the guideline has the same guiding significance.

1) Based on the operation frequency, select the proper height, initial length (l), and width (w) of the cavity unit according to the cavity theory

$$k_x^2 + k_y^2 + k_z^2 = k_0^2$$
$$k_x = \frac{\pi}{l}, \quad k_y = \frac{0.5 \times \pi}{w}, \quad k_z = 0$$
$$k_0 = \frac{2 \times \pi \times f_0}{c}.$$

2) Based on the desired gain, select the proper cavity unit number and overlapped width. Then, start modeling the antenna array using the commercial 3-D electromagnetic field solver (HFSS is used here): all the sidewalls are planar plates in this step.

3) Use the single-probe, center-fed approach to excite the antenna array. Adjust the width and length of the cavity unit together with the feeding location, making the width as small as possible under relatively good matching conditions, while guaranteeing that each cavity is operating at the TM_{1n0} ($n = 0.5$) mode.

4) Replace the planar sidewalls with the realistic via-hole sidewalls. Then optimize the width and length of the cavity unit and the feeding location.

IV. ANTENNA DESIGN AND MEASUREMENT RESULT

The geometry of the final realized five-unit HPO cavity cascaded antenna array is shown in Fig. 4. The dielectric used here is the 2-mm-thick F4B substrate. The length and width of the cavity unit are 33 and 9 mm, respectively. The overlapped width is 3 mm, and the feeding probe locates 5.4 mm away from the edge. All via holes including the feeding probe have a diameter of 0.5 mm. The hole spacing and the distance between the hole center to the board edge are both 1.5 mm. The overall dimension of the proposed antenna is $168 \times 18 \times 2$ mm^3.

The feeding structure is illustrated in Fig. 4(b) (enlarged inset): the feeding probe sits at a metal ring with a width of 0.5 mm; outside the metal ring, the circular ring with a width of 1 mm is the place where the lump port locates. As to practical implement, the inner conductor of a semirigid cable with a diameter of 0.51 mm crosses the circular ring and is soldered to the metal ring, while the outer conductor with a diameter of 2.2 mm is soldered to the center line all the way from the outer edge of the circular ring to one end.

The fabricated prototype is shown in Fig. 5. Reflection coefficient was measured using a N5071B vector network analyzer (300 kHz to 9 GHz), the gains and radiation patterns were measured in a far field anechoic chamber. The simulated
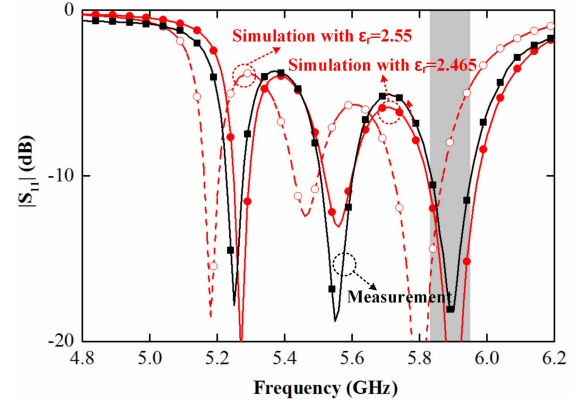

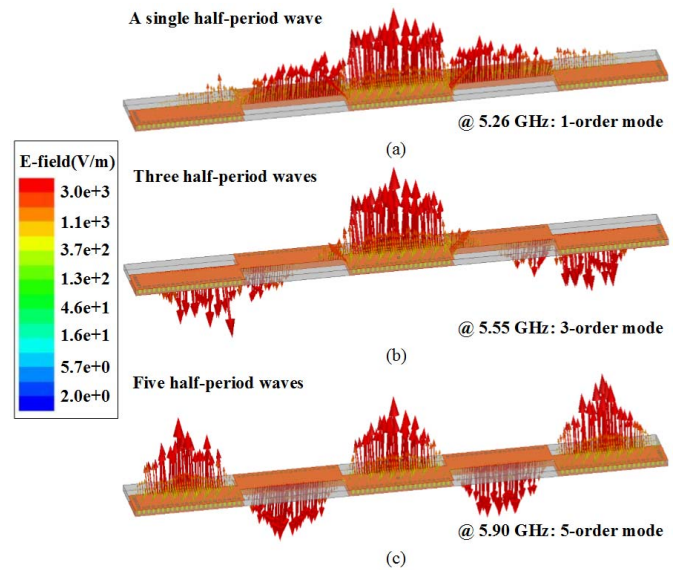Fig. 6. Measured and simulated magnitudes of reflection coefficients. Gray area: operation band.

Fig. 7. Simulated vector electric field distributions at (a) 5.26, (b) 5.55, and (c) 5.90 GHz.

and measured magnitude of reflection coefficients are shown in Fig. 6. Three resonant frequencies are observed, which are the first-, third-, and fifth-order modes [24]. The fifth-order mode is the operating mode, and the working bandwidth is denoted in Fig. 6 (gray area): the measured bandwidth is 120 MHz (2.04%, 5.83–5.95 GHz), while the original simulated bandwidth is 130 MHz (2.24%, 5.73–5.86 GHz). The center frequency deviates 100 MHz from the simulated 5.8 GHz to the measured 5.9 GHz. The reason is caused by the fact that the realistic permittivity value deviates from the nominal. When the permittivity is revised from 2.55 to 2.465, the simulated result as denoted in Fig. 6 (red solid line with solid circles) agrees well with the measurement: the simulated bandwidth after revision is 140 MHz centered at 5.9 GHz (2.37%, 5.83–5.97 GHz). In order to illustrate the field mode of each resonance, the simulated vector electric field distributions of the three resonances are given in Fig. 7. The three resonances with the center frequencies of 5.26, 5.55, and 5.90 GHz refer to the first-, third-, and fifth-order modes, indicating half, one and a half, and two and a half wavelength modes along the cavity array, respectively, as shown in Fig. 7(a)–(c). However, due to the lack
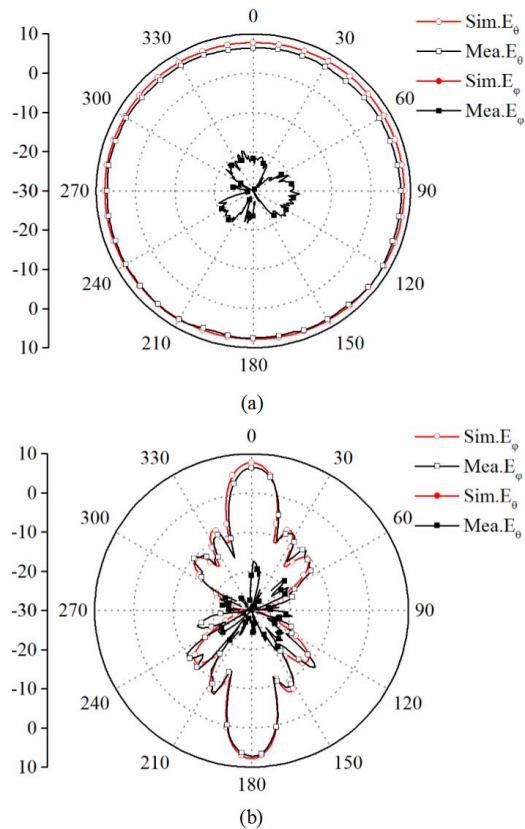
Fig. 8. Measured and simulated radiation patterns at 5.9 GHz in (a) E plane (yz) and (b) H plane (xz).
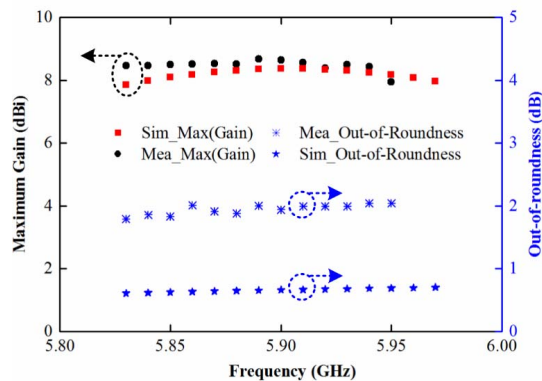

Fig. 9. Measured and simulated maximum gains and the out-of-roundness values.

of omnidirectional performance of the first- and third-order modes, the two lower resonances cannot be used to extend the impedance bandwidth.

The measured radiation patterns in the two principal planes at 5.9 GHz are given in Fig. 8, compared with the simulated results after revision. They agree well with each other. As seen, good omnidirectional patterns are obtained in the E plane (yz plane) and figure-8 patterns are achieved in the H plane (xz plane). The measured and simulated maximum gains and the out-of-roundness values are presented in Fig. 9. Among the bandwidth, the simulated maximum gains vary from 7.85 to 8.36 dBi, while the measured ones range from 7.94 to 8.67 dBi. The pattern is highly directive in the E plane, so the

placement of the antenna should be parallel to the x-axis restrictively. The simulated gain variation is less than 0.7 dB, while the measured one is less than 2.04 dB. The measured cross-pol levels are better than -18.2 and -17.4 dBi in the E and H plane, respectively. Thus, the proposed five-unit HPO cavity cascaded antenna array shows good performance.

V. CONCLUSION

A new structure of the cavity cascaded antenna array with HPO pattern is introduced. Based on the two-end-shorted PSL, by loading blocking structures alternatively and periodically, the rectangular open cavities operating at the TM_{1n0} ($n = 0.5$) mode are cascaded alternatively, forming a series of almost in-line magnetic currents, generating an omnidirectional pattern in the E plane. The proposed structure is scalable along one direction to achieve the omnidirectional pattern with a relatively high gain, and the gain increases with the decrease in height. An example of a five-unit cavity cascaded antenna array is presented and fabricated. It provides a bandwidth of 120 MHz and an HPO pattern with a gain variation of 1.94 dB from 6.7 to 8.64 dBi at 5.9 GHz.

REFERENCES

[1] K. L. Wong, F. Hsiao, and T. Chiou, "Omnidirectional planar dipole array antenna," *IEEE Trans. Antennas Propag.*, vol. 52, no. 2, pp. 624–628, Feb. 2004.

[2] Z. Zhang, M. F. Iskander, J. C. Langer, and J. Mathews, "Dual-band WLAN dipole antenna using an internal matching circuit," *IEEE Trans. Antennas Propag.*, vol. 53, no. 5, pp. 1813–1818, May 2005.

[3] K. Wei, Z. Zhang, W. Chen, Z. Feng, and M. Iskander, "A triband shunt-fed omnidirectional planar dipole array," *IEEE Antennas Wireless Propag. Lett.*, vol. 9, pp. 850–853, 2010.

[4] H. A. Wheeler, "A vertical antenna made of transposed sections of coaxial cable," *IRE Conv. Rec.*, vol. 4, pp. 160–164, Mar. 1956.

[5] K. Wei, Z. Zhang, Z. Feng, and M. F. Iskander, "A wide-band MNG-TL dipole antenna with stable radiation patterns," *IEEE Trans. Antennas Propag.*, vol. 61, no. 5, pp. 2418–2424, May 2013.

[6] C. Soras, M. Karaboikis, G. Tsachtsiris, and V. Makios, "Analysis and design of an inverted-F antenna printed on a PCMCIA card for the 2.4 GHz ISM band," *IEEE Antennas Propag. Mag.*, vol. 44, no. 1, pp. 37–44, Feb. 2002.

[7] D. Chizhik, J. Ling, and R. A. Valenzuela, "The effect of electric field polarization on indoor propagation," in *Proc. IEEE Int. Conf. Universal Pers. Commun. (ICUPC)*, vol. 1. Oct. 1998, pp. 459–462.

[8] A. Alford and A. G. Kandoian, "Ultrahigh-frequency loop antennas," *Elect. Eng.*, vol. 59, no. 12, pp. 843–848, Dec. 1940.

[9] H. R. Chuang, T.-S. Horng, J.-W. Pan, and C.-H. Wang, "OMNI-directional horizontally polarized Alford loop strip antenna," U.S. Patent 5 767 809, Jun. 16, 1998.

[10] C. C. Lin, L. C. Kuo, and H. R. Chuang, "A horizontally polarized omnidirectional printed antenna for WLAN applications," *IEEE Trans. Antennas Propag.*, vol. 54, no. 11, pp. 3551–3556, Dec. 2006.

[11] C. H. Ahn, S. W. Oh, and K. Chang, "A dual-frequency omnidirectional antenna for polarization diversity of MIMO and wireless communication applications," *IEEE Antennas Wireless Propag. Lett.*, vol. 8, pp. 966–969, 2009.

[12] Y. Yu, F. Jolani, and Z. Chen, "A wideband omnidirectional horizontally polarized antenna for 4G LTE applications," *IEEE Antennas Wireless Propag. Lett.*, vol. 12, pp. 686–689, 2013.

[13] X. L. Quan, R. L. Li, J. Y. Wang, and Y. H. Cui, "Development of a broadband horizontally polarized omnidirectional planar antenna and its array for base stations," *Prog. Electromagn. Res.*, vol. 128, pp. 441–456, Jun. 2012.

[14] A. L. Borja, P. S. Hall, Q. Liu, and H. Iizuka, "Omnidirectional loop antenna with left-handed loading," *IEEE Antennas Wireless Propag. Lett.*, vol. 6, pp. 495–498, 2007.

[15] X. Qing, C. K. Goh, and Z. N. Chen, "A broadband UHF near-field RFID antenna," *IEEE Trans. Antennas Propag.*, vol. 58, no. 12, pp. 3829–3838, Dec. 2010.

[16] X. Qing and Z. N. Chen, "Horizontally polarized omnidirectional segmented loop antenna," in *Proc. 6th Eur. Conf. Antennas Propag. (EUCAP)*, Mar. 2012, pp. 2904–2907.

[17] K. Wei, Z. Zhang, and Z. Feng, "Design of a wideband horizontally polarized omnidirectional printed loop antenna," *IEEE Antennas Wireless Propag. Lett.*, vol. 11, pp. 49–52, 2012.

[18] K. Wei, Z. Zhang, Z. Feng, and M. F. Iskander, "A MNG-TL loop antenna array with horizontally polarized omnidirectional patterns," *IEEE Trans. Antennas Propag.*, vol. 60, no. 6, pp. 2702–2710, Jun. 2012.

[19] X. Cai and K. Sarabandi, "A compact broadband horizontally polarized omnidirectional antenna using planar folded dipole elements," *IEEE Trans. Antennas Propag.*, vol. 64, no. 2, pp. 414–422, Feb. 2016.

[20] X. Qing, Z. N. Chen, and C. K. Goh, "A horizontally polarized omnidirectional slot antenna array," in *Proc. APS*, Chicago, IL, USA, Jul. 2012, pp. 1–2.

[21] T. S. P. See, X. Qing, and Z. N. Chen, "A wideband horizontally polarized omnidirectional antenna," in *Proc. IEEE 4th Asia-Pacific Conf. Antennas Propag.*, Kuta, Indonesia, Jun. 2015, pp. 294–295.

[22] Z. Zeng *et al.*, "The design and experiment of a dual-band Omnidirectional SIW slot array antenna," in *Proc. APMC*, Bangkok, Thailand, Dec. 2007, pp. 1–4.

[23] G. Hua, W. Hong, X. H. Sun, and H. X. Zhou, "Design of an omnidirectional line array with SIW longitudinal slot antenna," in *Proc. ICMMT*, Apr. 2008, pp. 1114–1117.

[24] L. Chang, Z. Zhang, Y. Li, and Z. Feng, "All-metal antenna array based on microstrip line structure," *IEEE Trans. Antennas Propag.*, vol. 64, no. 1, pp. 351–355, Jan. 2016.

A Simple Miniature Ultrawideband Magnetic Field Probe Design for Magnetic Near-Field Measurements

Zhaowen Yan, Jianwei Wang, Wei Zhang, Yansheng Wang, and Jun Fan

Abstract—A simple miniature magnetic-field probe for near-field measurements in 9-kHz–20-GHz bandwidth, which is applied to high-speed circuits, has been proposed and manufactured. The magnetic-field probe is built on a four-layer printed circuit board (PCB) using high-performance and low-loss Rogers material ($\varepsilon_r = 3.48$ and tan $\delta = 0.0037$). Electric field coupling can be suppressed by PCB shielding structure of the magnetic-field probe. Coax-thru-hole via array technique is used to achieve impedance match. The resonance in working frequency band is suppressed through via fence, making $|S_{21}|$ rather smooth in the operation band. Experimental results show that the working frequency band is up to 9 kHz–20 GHz.

Index Terms—Coax-thru-hole via array, near-field measurements, ultrawideband magnetic-field probe, via fence.

I. INTRODUCTION

With the rapid development of science and technology, microwave and integrated circuit are developing into the tendency of high density and integration, which leads to serious EMC problems [1] as a result of small space and high operation frequency. Mapping of near-field measurement is an effective method to locate radiation source [2], redesign circuits, and enhance EMC performance of electronic systems. Therefore, probe is a key component in near-field measurement. As is known, the electromagnetic interference generated by the radiation source has a very broad electromagnetic spectrum when the circuit or electronic system is working. Thus, broadband probe is increasingly crucial for near-field measurement.

Based on the planar magnetic field probe with a coplanar waveguide (CPW) feed line in [3], a resonance-suppressed magnetic field probe with tapered transition structure between square-loop aperture and 50-Ω CPW is proposed in [4]. However, the probe can be applied only in the range from 1 to 7 GHz. In [5], the tapered transition structure is moved to CPW transmission line, enhancing the working frequency band. In [6], a magnetic field probe based on thin-film process is proposed. The spatial resolution can be greatly enhanced, because loop aperture can be miniaturized through thin-film technology. However, the upper limit frequency is merely up to 10 GHz. A magnetic-field resonant probe [8] fabricated on a four-layer printed circuit board (PCB) does not satisfy the requirements of wideband measurement. The probe manufactured in low-temperature cofired ceramics [9] has a good performance of spatial resolution, working frequency band, and electric field suppression. But the structure of the probe is very complex and the cost is high.

Z. Yan, J. Wang, and W. Zhang are with the School of Electronic and Information Engineering, Beihang University, Beijing 100191, China (e-mail: yanzhaowen@buaa.edu.cn; wangjianwei18863@163.com; 1113867415@qq.com).

Y. Wang and J. Fan are with the EMC Laboratory, Missouri University of Science and Technology, Rolla, MO 65409 USA (e-mail: ywd8b@mst.edu; jfan@mst.edu).

Color versions of one or more of the figures in this communication are available online at http://ieeexplore.ieee.org.

Digital Object Identifier 10.1109/TAP.2016.2606556